This is the accepted manuscript made available via CHORUS. The article has been published as:

Scaling laws for two-dimensional dendritic crystal growth in a narrow channel

Younggil Song, Damien Tourret, and Alain Karma

Phys. Rev. E **107**, L052801 — Published 12 May 2023

DOI: 10.1103/PhysRevE.107.L052801

Scaling laws for two-dimensional dendritic crystal growth in a narrow channel

Younggil Song,[1,2] Damien Tourret,[3] and Alain Karma[1,*]

[1] *Department of Physics and Center for Interdisciplinary Research on Complex Systems, Northeastern University, Boston, MA 02115 USA*

[2] *Materials Science Division, Lawrence Livermore National Laboratory, Livermore, CA 94550, USA*

[3] *IMDEA Materials Institute, Getafe, 28906 Madrid, Spain*

(Dated: April 24, 2023)

We investigate analytically and computationally the dynamics of 2D needle crystal growth from the melt in a narrow channel. Our analytical theory predicts that, in the low supersaturation limit, the growth velocity V decreases in time t as a power law $V \sim t^{-2/3}$, which we validate by phase-field and dendritic-needle-network simulations. Simulations further reveal that, above a critical channel width $\Lambda \approx 5l_D$, where l_D the diffusion length, needle crystals grow with a constant $V < V_s$, where V_s is the free-growth needle crystal velocity, and approaches V_s in the limit $\Lambda \gg l_D$.

Solid-liquid interfaces exhibit different patterns depending on their growth conditions [1]. When unconstrained, i.e. growing freely in an infinite domain at a given driving force (e.g. undercooling, supersaturation), a dendritic crystal is known to reach a steady growth velocity. The growth velocity and tip morphology of such a free dendrite are given by combining solute and/or heat conservation [2] with the solvability condition that incorporates the effect of the anisotropy of the interface excess free energy of the solid-liquid interface (surface tension) [3–6]. When the dendrite is free of lateral interactions from neighboring crystal, secondary (or higher-order) branches can emerge due to thermal fluctuations [7–11], which leads to the formation of complex microstructures. In contrast, the constrained growth of a dendrite within a channel reduces to the well-known Saffman-Taylor problem [4, 12–17]. The resulting crystal shape is a symmetric finger or an unstable widening cell above or below a critical undercooling, respectively [16–19]. The threshold between these morphologies are linked to the surface tension [16–18].

Theoretical and numerical investigations of 2D and 3D crystal growth in a channel [4, 12–17, 20, 21] have mostly focused on the dendrite tip morphology for a high undercooling (Δ) or solute supersaturation (Ω). Exploring lower undercoolings, two-dimensional phase-field studies [19] have shown that a dendrite in a channel slows down with a power-law of time below an undercooling $\Delta = 0.5$, along with a widening of the tip. For a higher Δ, the dendrite shows a steady state growth with a symmetric dendrite tip. The transition between the two growth regimes is close to the morphological threshold $\Delta = 0.49$ of a symmetrical finger [17, 18].

While these studies have shown the existence of these two growth regimes (power-law deceleration and a steady state growth) [19, 20], an analytical theory for the decelerating dynamics and the transition between regimes remains lacking. In this letter, we study the growth of a 2D binary alloy dendrite in a channel for a low solute supersaturation Ω — readily generalizable to the growth of a pure element at a low undercooling Δ. We derive an analytical law for the growth of the confined dendrite by combining the solvability condition [3–6] and solute conservation considering a sharp needle-like crystal [22]. Our analytical derivation predicts that the dendrite slows down with time t as $V \sim At^{-2/3}$, where the prefactor A depends directly and nonlinearly upon the channel width Λ. We verify the theory via two numerical approaches, namely using phase-field (PF) [28, 29] and the dendritic-needle-network (DNN) models [22, 35].

The PF approach is a powerful computational method to simulate complex interface dynamics in various phenomena [23, 24]. The method relies on a "phase field", or order parameter, which has a given value within different phases or grains, and varies continuously through interfaces. In solidification, taking into account anisotropic properties of solid-liquid interfaces, PF simulations can reproduce the evolution of complex anisotropic structures [25, 26]. An asymptotic analysis permits the use of a diffuse interface much wider than the actual physical interface [27]. For an alloy, the introduction of an "anti-trapping" term corrects the numerically-induced solute trapping due to the artificially wide interface, thus ensuring quantitative and computationally-efficient predictions [28, 29]. Combined with additional numerical techniques, such as parallelization and nonlinear preconditioning [30], resulting calculations provide quantitative simulations in two (2D) and three (3D) dimensions, at time and length scales directly comparable to experiments [31–34].

The DNN model [22, 35] was developed to simulate dendrite growth at low Ω. In this regime, PF simulations are challenging, due to the extreme separation of scale between the dendrite tip radius ρ and the solute diffusion length $l_D \equiv D/V$, where D is the diffusivity in the liquid and V is the dendrite tip velocity. While PF typically requires a grid spacing much lower than the dendrite tip radius, DNN simulations remain accurate using a grid spacing close to, or even above, a dendrite tip radius [22, 35], which provides a great computational advantage.

The DNN model consists of solving the transport of the

* Corresponding author: a.karma@northeastern.edu

solute field u in the liquid phase (e.g., the diffusion equation), interacting with a hierarchical network of needle-like branches at equilibrium. The growth velocity of each dendritic tip is obtained by combining solute balances at two distinct length scales [22]. At a scale $\gg \rho$, curvature effects can be neglected and a dendritic branch can be represented as a sharp line segment at fixed equilibrium concentration $u = 0$. On the other hand, at a scale $\ll l_D$, the solute field relaxes fast enough to assume a Laplacian u field in the vicinity of the tip. The analytical solution to this problem [37] exhibits a square-root singularity of the normal gradient of the field in the vicinity of the tip with a "flux intensity factor" $\mathcal{F}$ that is a measure of the incoming flux towards the dendrite tip. Using an analogy with fracture mechanics, namely with the stress field ahead of a crack tip submitted to anti-plane shear (mode III) loading, $\mathcal{F}$ can be calculated with the J-integral commonly used in fracture mechanics [22, 38, 39]. The resulting conservation equation reads

$$\rho V^2 = \frac{2D^2\mathcal{F}^2}{d_0}\,, \tag{1}$$

where d_0 is the capillary length. By combining the above equation and the solvability condition [3–6],

$$\rho^2 V = \frac{2Dd_0}{\sigma}\,, \tag{2}$$

where σ is the tip selection parameter fixed by the interface anisotropy [5], the tip radius and growth velocity of a needle tip is given by [22]

$$\frac{\rho(t)}{d_0} = \left[\frac{2}{\sigma^2\mathcal{F}(t)^2}\right]^{1/3}, \tag{3}$$

$$\frac{V(t)d_0}{D} = \left[2\sigma\mathcal{F}(t)^4\right]^{1/3}. \tag{4}$$

The transient evolution of the solute field around the dendrite tip is captured by the time-dependent $\mathcal{F}(t)$.

For a needle-like dendrite at $\Omega \ll 1$, the 2D Ivantsov solution [2] reduces to $\Omega \approx \sqrt{\pi \mathrm{Pe}}$, where $\mathrm{Pe} = \rho V/(2D)$ is the Péclet number. Then, the steady radius ρ_s and velocity V_s of a free dendrite become [22]

$$\frac{\rho_s}{d_0} = \frac{\pi}{\sigma\Omega^2}\,, \tag{5}$$

$$\frac{V_s d_0}{D} = \frac{2\sigma\Omega^4}{\pi^2}\,. \tag{6}$$

Let a needle-like dendrite grow within a channel of width Λ. For $\Lambda \ll l_D$, the solute field surrounding the needle tip is essentially Laplacian with $\nabla^2 u = 0$. Applying the J-integral around the tip in a channel yields that $\mathcal{F}(t)$ depends on the solute gradient, $\partial u/\partial x$, ahead of the tip in the needle growth direction x as [22, 38, 39]

$$\mathcal{F}(t)^2 = \frac{\Lambda d_0}{2\pi}\left(\frac{\partial u}{\partial x}\right)^2. \tag{7}$$

For $\Lambda \ll l_D$, the solute concentration profile can also be considered one-dimensional (1D), such that the gradient in front of the needle follows the Zener approximation [2, 40]

$$\frac{\partial u}{\partial x} \approx \frac{\Omega}{\sqrt{\pi D t}}\,. \tag{8}$$

Combining these last two equations with Eq. (4), the needle tip velocity can be expressed as

$$V(t) = \left(\frac{\sigma\Lambda^2}{2\pi^4}\frac{D}{d_0}\Omega^4\right)^{1/3} t^{-2/3}\,. \tag{9}$$

Normalizing time and space using theoretical steady-state values of ρ_s (Eq. (5)) and V_s (Eq. (6)) leads to

$$\widetilde{V}(\tilde{t}) = \frac{V(t)}{V_s} = \left(\frac{\widetilde{\Lambda}}{2\pi\tilde{t}}\right)^{2/3}, \tag{10}$$

where $\tilde{t} = tV_s/\rho_s$ and $\widetilde{\Lambda} = \Lambda/\rho_s$.

In order to validate the scaling law (10) for a dendrite growing in a narrow channel at low Ω, we first performed both PF and DNN simulations at $\Omega = 0.05$, whose results

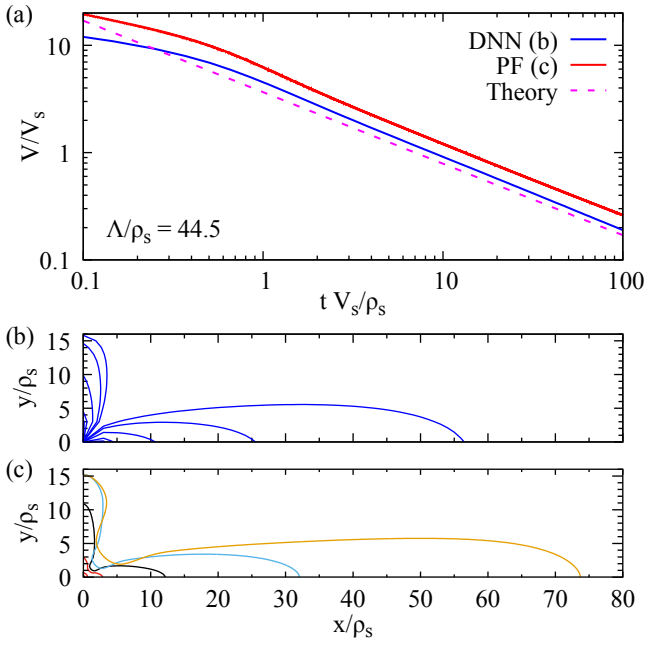


FIG. 1. Calculated growth velocities (a) and morphological evolution (b)-(c) of a dendrite in a channel of width $\widetilde{\Lambda} = 44.5$ at a solute supersaturation $\Omega = 0.05$. Both DNN (blue solid line) and PF (red solid line) results exhibit a power law close to the analytical theory, Eq. (10) (pink dashed line). Morphologies in (b) and (c) show solid-liquid interface locations at $\tilde{t} = 0.01$, 0.1, 1, 10, and 100 from the DNN and PF simulations, respectively. In panel (c), different colors denote different times $\tilde{t} < 1$ (red), $\tilde{t} = 1$ (black), 10 (cyan), and 100 (yellow).

for $\widetilde{\Lambda} = 44.5$ are shown in Fig. 1(a). Both PF (red solid line) and DNN (blue solid line) predictions follow Eq. (10) (pink dashed line). While the DNN needle effectively remains a sharp line interacting with the solute field, its virtual thickness can still be estimated by time integration of the fluxes along its sides (see details in Supplementary Material [41] and Ref. [22]). The resulting interface and its time evolution, shown at $\tilde{t} = 0.01, 0.1, 1, 10$, and 100 in Fig. 1(b), agrees reasonably with the interface predicted by the PF method (Fig. 1(c)).

Because the DNN dendrite remains infinitely sharp, thus matching the underlying assumption of Eq. (10), the DNN-predicted velocity has a prefactor closer to that of Eq. (10) than that from the PF simulation. In the latter, the dendrite actually thickens, thus partially filling the channel and effectively increasing the solute gradient in the x direction and yielding a higher velocity than that predicted for a sharp needle. These results are consistent with previous PF studies [19, 20], which showed that the power law deceleration observed at a relatively low Péclet number disappeared when the undercooling

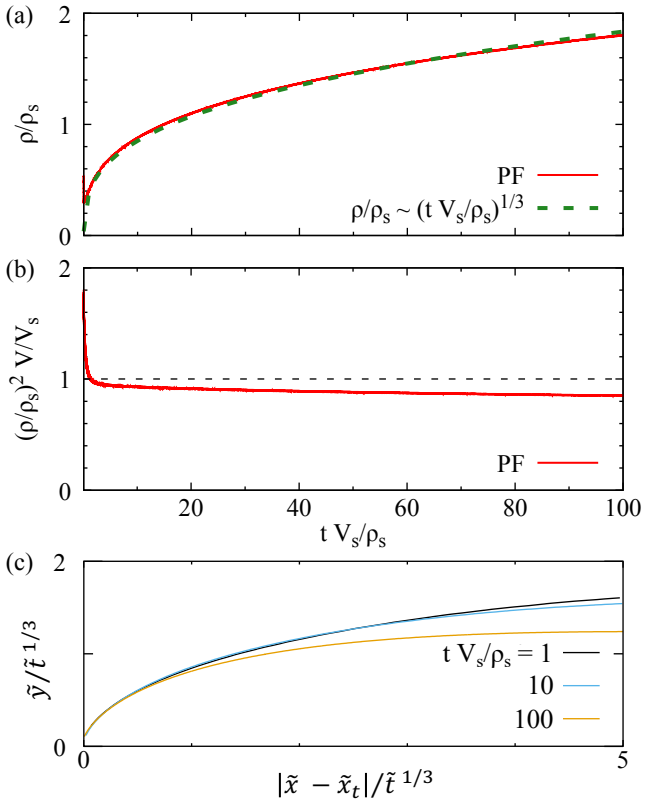


FIG. 2. Time-dependent tip radius $\tilde{\rho}$ (a) and $\tilde{\rho}^2\widetilde{V}$ (b) of a dendrite in $\widetilde{\Lambda} = 44.5$ at $\Omega = 0.05$. Panel (a) shows $\tilde{\rho}$ from the PF simulation of Fig. 1 (red line) compared to a power law $\sim \tilde{t}^{1/3}$ (green dashed line). In (b), $\tilde{\rho}^2\widetilde{V}$ of the PF dendrite within a narrow channel (red line) is compared to the expected value of 1 (thin dashed line) for a free dendrite. Panel (c) compares the scaled tip morphologies $\tilde{y}/\tilde{t}^{1/3}$ against $|\tilde{x}-\tilde{x}_t|/\tilde{t}^{1/3}$ at three different times $\tilde{t} = 1$ (black), 10 (cyan), and 100 (yellow).

was increased and the dendrite was progressively filling up the channel.

In the PF simulation of Fig. 1(c), the evolution of the dendrite tip radius and its morphology are also relevant to the filling of the channel. As shown in Fig. 2(a), the tip radius of the confined dendrite (red solid line) increases as $\tilde{\rho} \sim \tilde{t}^{1/3}$ (green dashed line), which is consistent with the constancy of $\rho^2 V$ predicted by solvability theory [3–6]. Indeed, the calculated evolution of $\rho^2 V$, plotted as red line in Fig. 2(b), quickly approaches a constant value slightly lower but close to $\tilde{\rho}^2\widetilde{V} = 1$ (black dashed line), i.e., close to the free dendrite steady state with $\rho \approx \rho_s$ and $V \approx V_s$ [22, 47]. For the confined dendrite, $\tilde{\rho}^2\widetilde{V}$ appears to decrease slowly soon after it reaches $\tilde{\rho}^2\widetilde{V} \approx 1$, but remains close to 1 during the entire simulation.

Since the tip velocity evolves as $\widetilde{V} \sim \tilde{t}^{-2/3}$, the tip position $\tilde{x}_t$ increases as $\tilde{x}_t \sim \tilde{t}^{1/3}$, i.e., with a similar power law as the tip radius, $\tilde{\rho} \sim \tilde{t}^{1/3}$. One can thus assess whether the dendrite tip retains a self-similar shape over time by plotting $|\tilde{x} - \tilde{x}_t|/\tilde{t}^{1/3}$ against $\tilde{y}/\tilde{t}^{1/3}$, as done in Fig. 2(c). There, the scaled dendrite shapes at different times $\tilde{t} = 1$ (black), 10 (cyan), and 100 (yellow) show that the immediate vicinity of the tip remains almost unchanged. However, later in the simulation, as the dendrite starts to fill the channel (e.g., $\tilde{t} = 100$), the effect of confinement becomes apparent with a relatively narrower shape of the dendrite further from the tip.

In order to investigate the effect of the dendrite volume (area) on its growth dynamics, we performed additional PF simulations with channel widths $\widetilde{\Lambda} = 4.2$ and 10.9. In Fig. 3(a), $\widetilde{V}$ is scaled by $\widetilde{\Lambda}^{2/3}$, in order to represent all simulations on the same graph, comparing them with the expected $\widetilde{V}/\widetilde{\Lambda}^{2/3} = (2\pi\tilde{t})^{-2/3}$ (pink dashed line) from Eq. (10). Solid lines show results with $\widetilde{\Lambda} \simeq 44.5$ (red), 10.9 (green), and 4.2 (purple). A wider channel results in a longer initial transient time. Nevertheless, once a power-law regime is reached ($\tilde{t} \geq 1$) the widest channel leads to the best agreement with Eq. (10).

Interface shapes at $\tilde{t} = 0.01$, 0.1, 1, 10, and 100 are drawn in Fig. 3(b)-(d) for $\widetilde{\Lambda} = 44.5$, 10.9, and 4.2, respectively, with space coordinates normalized by the channel half-width. As expected, narrower channels (Fig. 3(d)) get filled by the dendrite faster than wider channels. These results confirm that, for a given Ω, the dendrite velocity deviates from the proposed growth law when Λ decreases, as the assumption that $\Lambda \gg \rho$ is no longer valid.

Regardless of the channel width, dendrites slow down with an exponent close to the predicted $V \sim t^{-2/3}$ law. Once the effect of confinement becomes predominant, as long as $\rho \ll \Lambda$, the constancy of $\rho^2 V$ [3–6] implies that ρ increases with a corresponding $\rho \sim t^{1/3}$ as shown in Fig. 2(a). Hence, as ρ increases, the problem approaches that of a 1D planar interface, known to follow $V \sim t^{-1/2}$ [16, 40, 48]. Hence, even though dendrites in Fig. 3 are expected to retain a finger morphology rather than asymptotically tending toward a planar interface,

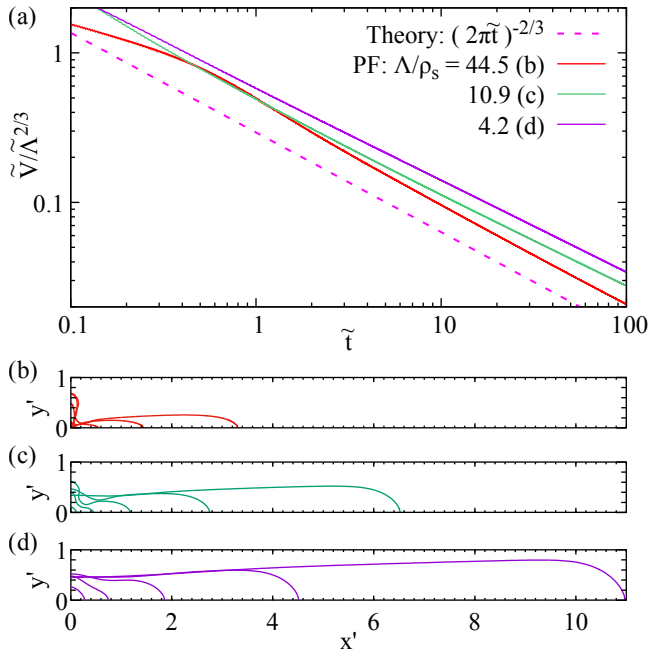


FIG. 3. PF-predicted growth velocities (a) and morphological evolutions (b-d) of dendrites for different channel widths $\widetilde{\Lambda} = 44.5$ (red), 10.9 (green), and 4.2 (purple solid line), compared to the analytical law with $\widetilde{V} \sim \tilde{t}^{-2/3}$ (pink dashed line). Panels (b), (c), and (d) show snapshots of the interface locations at $\tilde{t} = 0.01$, 0.1, 1, 10, 100 for $\widetilde{\Lambda} = 44.5$, 10.9 and 4.2, respectively. They are scaled with respect to $\Lambda/2$, i.e., with $x' = 2x/\Lambda$ and $y' = 2y/\Lambda$.

the higher exponent exhibited by the thicker dendrites (i.e. narrower channel, e.g. Fig. 3(d)) likely indicates an intermediate state between dendritic ($V \sim t^{-2/3}$) and planar ($V \sim t^{-1/2}$) growth.

If the channel is very wide, the resulting free dendrite should not be affected by the domain boundaries and thus reach a steady state velocity $\widetilde{V} = 1$. Consequently, for a given supersaturation, we expect that there exists a critical channel width Λ_c that delimits these two growth regimes. We performed simulations with various Λ at a given Ω in order to identify Λ_c, namely with $\Omega = 0.2$ (PF) and $\Omega = 0.2$, 0.1, and 0.05 (DNN). The diffusive interaction between the dendrite and the channel boundaries is expected to be the key mechanism that determines whether the dendrite will decelerate or reach a steady state. Hence, results presented in Fig. 4 are scaled with respect to the diffusion length l_D. For $\Omega = 0.2$, 0.1, and 0.05, the diffusion lengths of a free dendrite are $l_D/\rho_s = 39.3$, 157.1, and 628.3, respectively.

In PF simulations (Fig. 4(a)), growth velocities in the three narrowest channels, namely $\Lambda/l_D = 0.3$, 0.7 and 1.4 (red dashed lines) decelerate towards the proposed power law. As observed earlier, as Λ is wider, it takes a longer time to reach the $\tilde{t}^{-2/3}$ growth regime. In particular, at $\Lambda/l_D = 2.7$ (lightest red dashed line), the dendrite is still well within a transition regime towards the power law at the end of the simulation. On the other hand, the dendrite velocity for $\Lambda/l_D = 5.5$ (blue solid line) does not show any inflexion during the simulated time, and seems to approach a steady-state velocity.

DNN simulations allow us to explore a broader range of parameters, and show the similar results, namely with $\Omega = 0.2$, 0.1, and 0.05. Results, shown in Fig. 4(b)-(d), exhibit the same behavior as in PF simulations (Fig. 4(a)). Dendrites in narrower channels (red dashed lines) slow down towards the theoretical power law. Meanwhile, dendrites in wider channels (blue solid lines) reach a constant growth velocity. At $\Omega = 0.05$, the distinction between decelerating and steady regime is not obvious within the time range represented in Fig. 4(d), but it appears unambiguously looking at longer simulations [41].

Both PF and DNN results exhibit two distinct growth behaviors: the power law deceleration at low Λ and a steady state growth at higher Λ. The crossover between the two distinct growth dynamics occurs at $2.7 < \Lambda_c/l_D < 5.5$ in PF simulations and at $4.8 < \Lambda_c/l_D < 5.1$ according to DNN results. We conclude that the critical channel width Λ_c is approximately $5\,l_D$. Interestingly, this crossover at $\Lambda \approx 5\,l_D$ is consistent with other results showing that the transition between quasi-2D confined growth and 3D growth regimes occurs at a sample height of approximately $5\,l_D$ in 3D DNN simulations [36].

One unexpected observation from Fig. 4 is that, at $\Lambda > \Lambda_c$, dendrites can reach a steady state velocity that is notably smaller than V_s. In such cases, the channel boundaries still interact with the dendrite even if Λ is wide enough for a dendrite to reach a steady state. In our simulations, the reached steady state velocity are as low as about $0.6V_s$. The channel width necessary for the dendrite to stabilize at a steady velocity close to the free dendrite theoretical velocity V_s can be as high as over a hundred times the diffusion length at relatively high $\Omega = 0.2$, as seen in Fig. 4(b). As a dendrite approaches a steady state, its tip morphology is also stabilized. The dendrite morphology can thus be described using the solvability condition in Eq. (2) [3–6] or other approaches [10, 11, 49, 50].

In summary, we developed an analytical theory for transient dendrite growth in a channel that predicts the power law deceleration $V \sim t^{-2/3}$. This result adds to our theoretical understanding of transient dendrite growth, which has been so far limited to early stage growth in an unconstrained geometry (described by the scaling law $V \sim t^{-2/5}$) [49]. Both PF and DNN simulations of dendritic growth within a narrow channel show that this power law holds as long as the channel width Λ is larger than the dendrite tip radius ρ. PF simulations show that, as the dendrite slows down, following solvability theory [3–6], its radius increases, the filling of the channel by the dendrite increases, and the velocity exponent rises above $-2/3$, thus getting closer to that expected for a planar interface ($V \sim t^{-1/2}$). On the other hand, when Λ is larger than a critical width $\Lambda_c \approx 5l_D$,

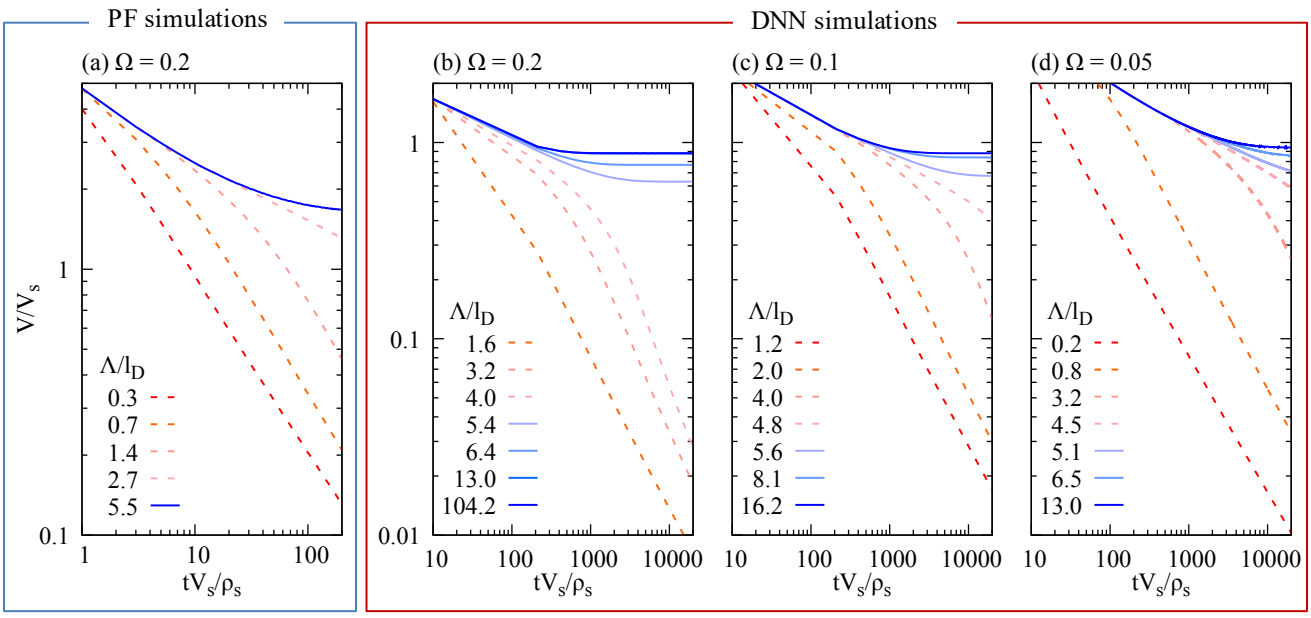


FIG. 4. Growth velocities of a dendrite within different channel widths Λ. (a) shows PF results at Ω = 0.2; (b), (c), and (d) show DNN results at Ω = 0.2, 0.1, and 0.05, respectively. The channel widths are scaled with respect to the diffusion length l_D/ρ_s = 39.3, 157.1, and 628.3 for Ω = 0.2, 0.1, and 0.05, respectively. Within a narrow channel, the dendrite is decelerated with the power law (red dashed lines). Otherwise, it approaches a steady state (blue solid lines).

dendrites can reach a steady state with a constant velocity. When Λ is slightly higher than Λ_c, the dendrite can stabilize at a velocity lower than V_s. This velocity increases towards V_s as Λ increases.

Results of this work may be related to the coarsening dynamics of parallel dendritic arms, e.g., after morphological destabilization of a planar interface or among dendritic sidebranches. In such case, an effective channel width is imposed by the presence of neighbor branches, and the growth kinetics of eliminated (i.e., slowing down) branches should follow the $V \sim t^{-2/3}$ power law identified here, until enough branches are eliminated and the spacing among active branches reaches the identified threshold of $\approx 5l_D$. Ongoing work on extending the present study to the coarsening dynamics of dendritic sidebranches, and resulting scaling laws for grain envelope shapes, will be presented elsewhere.

This study remains to be extended to three dimensions. PF studies revealed that 3D growth in a narrow channel also exhibits a power law deceleration [20] with a gradual transition toward a steady growth velocity [20, 36]. The lack of known analytical solution for the diffusion field surrounding an infinitely sharp needle — similar to that used in 2D in this Letter — makes the current approach not readily applicable, such that an analytical description of the deceleration regime and the corresponding critical width in 3D remains missing.

ACKNOWLEDGEMENT

This research was primarily supported by NASA grants NNX16AB54G and 80NSSC19K0135. D.T. acknowledges financial support from the Spanish Ministry of Science through the Ramon y Cajal grant RYC2019-028233-I. Y.S. acknowledges that this work was partially performed under the auspices of the U.S. Department of Energy by Lawrence Livermore National Laboratory under Contract DE-AC52-07NA27344.

[1] W. Kurz, D.J. Fisher, R. Trivedi, Int. Mater. Reviews 64, 311-354 (2019).
[2] G.P. Ivantsov, *Dokl. Akad. Nauk SSSR* **58**, 567-569 (1947).
[3] J. S. Langer, Lectures on the Theory of Pattern Formation, Chance and Matter (Les Houches, Session XLVI), edited by Souletie J., Bannimenus J. and R. Stora, Amsterdam, North-Holland, p. 629 (1987).
[4] J. S. Langer, Science **243**, 1150-1156 (1989).
[5] A. Barbieri and J. S. Langer, Rhys. Rev. A **39**, 5314-5325 (1989).
[6] M. Ben Amar and E. Brener, Phys. Rev. Lett. **71**, 589-592 (1993)
[7] R. Pieters and J. S. Langer, Phys. Rev. Lett. **56** 1948-1951 (1986).
[8] M. N. Barber, A. Barbieri and J. S. Langer, Phys. Rev. A **36**, 3340-3349 (1987).
[9] J. S. Langer, Phys. Rev. A **36**, 3350-3358 (1987).

[10] E. Brener, Phys. Rev. Lett. **71**, 3653-3656 (1993).
[11] E. Brener and D. Temkin, Phys. Rev. E **51**, 351-359 (1995).
[12] D. A. Kessler, J. Koplik, and H. Levine, Phys. Rev. A **34**, 4980-4987 (1986).
[13] E. A. Brener, M. B. Geilikman, and D. E. Temkin, Sov. Phys. JETP **67**, 1002-1009 (1988)
[14] Y. Couder, N. Gerard, and M. Rabaud, Phys. Rev. A **34** 5175-5178 (1986).
[15] M. Ben Amar and E. Brener, Phys. Rev. Lett. **75**, 561-564 (1995).
[16] E. Brener, H. Müller-Krumbhaar, Y. Saito, and D. Temkin, Phys. Rev. E **47**, 1151-1155 (1993).
[17] R. Kupferman, D. A. Kessler, and E. Ben-Jacob, Physica (Amsterdam) 213A, 451-464 (1995).
[18] E. A. Brener and D. A. Kessler, Phys. Rev. Lett. **88**, 149601 (2002).
[19] M. Sabouri-Ghomi, N. Provatas, and M. Grant, Phys. Rev. Lett. **86**, 5084-5087 (2001).
[20] H. Xing, P. P. Duan, X. L. Dong, C. L. Chen, L. F. Du and K. X. Jin, Philosophical Magazine **95**,1184–1200 (2015).
[21] K. Kassner, R. Guérin, T. Ducousso, and J.-M. Debierre, Phys. Rev. E **82** 021606 (2010).
[22] D. Tourret and A. Karma, Acta Mater. **61**, 6474-6491 (2013).
[23] L. Q. Chen, Ann. Rev. Mater. Res. **32**, 113-140 (2002).
[24] W. J. Boettinger, J. A. Warren, C. Beckermann, and A. Karma, Ann. Rev. Mater. Res. **32**, 163-194 (2002).
[25] R. Kobayashi, Physica D **63**, 410-423 (1993).
[26] B. Echebarria, A. Karma, and S. Gurevich, Phys. Rev. E **81**, 021608 (2010).
[27] A. Karma and W. J. Rappel , Phys. Rev. E **57**, 4323-4349 (1998).
[28] A. Karma, Phys. Rev. Lett. **87**, 115701 (2001).
[29] B. Echebarria, R. Folch, A. Karma, and M. Plapp, Phys. Rev. E **70**, 061604 (2004).
[30] K. Glasner, J. Comp. Phys. **174**, 695-711 (2001).
[31] N. Bergeon, D. Tourret, L. Chen, J.-M. Debierre, R. Guérin, A. Ramirez, B. Billia, A. Karma and R. Trivedi, Phys. Rev. Lett. **110**, 226102 (2013).
[32] D. Tourret and A. Karma, Acta Mater. **82**, 64-83 (2015).
[33] A. J. Clarke, D. Tourret, Y. Song, S. D. Imhoff, P. J. Gibbs, J. W. Gibbs, K. Fezzaa, A. Karma, Acta Mater. **129**, 203-216 (2017).
[34] D. Tourret, Y. Song, A.J. Clarke, A. Karma, Acta Mater. **122**, 220-235 (2017).
[35] D. Tourret, A. Karma, Acta Mater. **120**, 240-254 (2016).
[36] P.A. Geslin, C.-H. Chen, A. M. Tabrizi, A. Karma, Acta Mater. **202**, 42-54 (2021); C.-H. Chen, A. M. Tabrizi, P.A. Geslin, A. Karma, Acta Mater. **202**, 463-477 (2021).
[37] B. Derrida and V. Hakim, Phys. Rev. A **45**, 8759-8765 (1992).
[38] M. Ben Amar, J. R. Rice, J. Fluid Mech. **461**, 321-341 (2002).
[39] J. R. Rice, J. Appl. Mech. **35**, 379-386 (1968).
[40] C. Zener, J. Appl. Phys. **20**, 950-953 (1949).
[41] See Supplementary Material at (LINK) for numerical methods and simulation results supporting Fig. 4(d), which includes Refs. [42–46]
[42] R. González-Cinca, Y. Couder, and A. Hernández-Machado Phys. Rev. E **71**, 051601 (2005).
[43] C. Guo, J. Li, H. Yu, Z. Wang, X. Lin, J. Wang, Acta Mater. **136**, 148-163 (2017).
[44] D. Tourret, J.-M. Debierre, Y. Song, F. L. Mota, N. Bergeon, R. Guérin, R. Trivedi, B. Billia, A. Karma, Phys. Rev. E **92**, 042401 (2015).
[45] D. Tourret, M.M. Francois, A.J. Clarke, Comput. Mater. Sci. **162**, 206-227 (2019).
[46] W. Kurz, D. J. Fisher, *Fundamentals of solidification*, 3rd ed. (Trans Tech, Aedermannsdorf, 1992).
[47] M. Plapp and A. Karma, Phys. Rev. Lett. **84**, 1740-1743 (2000).
[48] P. Pelce, Europhys. Lett. **7**, 453-457 (1988).
[49] R. Almgren, W.S. Dai and V. Hakim, Phys. Rev. Lett. **71**, 3461-3464 (1993).
[50] D. V. Alexandrov, P. K. Galenko, Phil. Trans. R. Soc. A **378**, 20190243 (2020); D. V. Alexandrov, L. V. Toropova, E. A. Titova, A. Kao, G. Demange, P. K. Galenko, M. Rettenmayr, Phil. Trans. R. Soc. A **379**, 20200326 (2021).